Ultrathin Underwater Sound-Absorbing Metasurface by Coupling Local Resonance with Cavity Resonance

Jiaming Feng, Qingxuan Liang,* Yu Dou, Jingru He, Jin He, and Tianning Chen
School of Mechanical Engineering, Xi'an Jiaotong University, Xi'an 710049, China

(Received 17 December 2021; revised 7 February 2022; accepted 5 July 2022; published 21 September 2022)

An ultrathin underwater metasurface with low frequency, broadband, high-efficiency absorption, and high-hydrostatic-pressure-resistance performance is proposed based on the integrated principle of local resonance and cavity resonance. The design-parameter complexity is overcome by the global-optimization capability of the genetic algorithm. As a demonstration, an average sound-absorption coefficient of 92.3% at 500–10 000 Hz with an ultrathin thickness of 32 mm is achieved, including more than 99% sound-absorption coefficient at 4670–8630 Hz. In the proposed metasurface, the complex surface impedances of the three subsurfaces provide unique views for the high-efficiency sound-absorption coupling mechanism by the equivalent-circuit model. Further investigation demonstrates that the excellent property of high-efficiency sound absorption is maintained under 4.5-MPa hydrostatic pressure. The proposed metasurface provides more possibilities for underwater noise suppression.

DOI: 10.1103/PhysRevApplied.18.034054

I. INTRODUCTION

The stealth capability of submarines is crucial for underwater navigation. In recent decades, the design of the anechoic layer has gradually developed into an effective method for absorbing underwater sound, including reducing target intensity and suppressing radiated noise. A large number of studies have been carried out on underwater sound-absorption metasurfaces by referring to research on phononic crystals, including the resonance-coupling effect on band-gap widening [1]; the local-resonance mechanism on sound absorption [2]; the broadening method of the sound-absorption peak by multigradient scatters [3]; the underwater antireflection characteristics [4]; and the effects of multiresonators [5–8], voids [6–10], and backboards [6–8,10] on underwater sound absorption. The polymers of rubber, polyurethane, epoxy [11], etc. are mainly selected as matrix materials for the underwater sound-absorption metasurface to achieve impedance matching with water. However, the ideal absorption effect is difficult to achieve due to the low loss of the matrix material. Microparticles, glass beads, and carbon fibers [12–14] are added to improve the matrix-material loss, but a high-absorption peak remains exclusive. The local-resonance method [2,15–19], filling soft matrix materials with large-mass-density materials, breaks the mass-density law and achieves a high sound-absorption coefficient in a specific sound-absorption frequency band. Similarly, the cavity-resonance method [20–26], bringing different-shaped air cavities into the matrix material, plays two roles in reducing the stiffness of the matrix material and increasing the sound-reflection path in the matrix material. The reduction of stiffness is conducive to the improvement of sound absorption at low frequency, and the increase of the reflection path triggers a variety of resonance modes to improve the absorption coefficient at high frequency. However, neither the local-resonance method nor the cavity-resonance method has the effect of broadband sound absorption. Moreover, lower density and lower elastic modulus of the matrix materials are obviously insufficient to resist the hydrostatic pressure.

In recent years, a number of design methods for underwater sound-absorption metasurfaces have been proposed [3,12,16,20,27–33]. For the cavity-resonance principle, Zhang *et al.* [20] used semianalytical methodology to accurately predict the sound-absorption coefficient of anechoic coatings (40 mm) with an arbitrary cavity shape. The broadband sound absorption of a conical cavity and a cylindrical cavity in the range of 0–10 000 Hz were verified experimentally. Wang *et al.* [12] found that the sound-absorption coefficient at 2400–10 000 Hz was greater than 90% under a hydrostatic pressure of 1.5 MPa using the conical cavity metasurface (65 mm), and a high hydrostatic pressure resistance was realized due to the support of the carbon-fiber wall. For the local-resonance principle, Zhang and Cheng [32] optimized structural parameters for a multiple-gradient-scatter metasurface (60 mm) with excellent low-frequency sound absorption by adopting different optimization strategies of the Nelder-Mead algorithm and achieved an average sound-absorption

*liangqx728@xjtu.edu.cn

coefficient greater than 82% at 0–6000 Hz. Gao and Zhang [31] converted longitudinal waves to shear waves with greater loss by embedding a spiral structure in the highly viscoelastic soft-rubber matrix (220 mm), which achieved high sound absorption at 0–1000 Hz. In some innovative designs referring to classical air acoustic theories, Duan *et al.* [29] realized absorption coefficients greater than 90% at 306–921 Hz by introducing a rubber coating and an embedded neck into the classical Helmholtz resonance resonator (50 mm), including a wide band with nearly perfect sound absorption. Wu *et al.* [30] designed a different spiral underwater sound-absorption metasurface (50 mm) based on the generalized Snell reflection law, and the position of the quasiperfect absorption peak could be adjusted by varying the structural parameters. Overall, the design of an underwater sound-absorption metasurface with low-frequency, broadband, and high-efficiency absorption with preserved high-hydrostatic-pressure resistance is still a huge challenge.

Here, an integrated design method is proposed for an ultrathin metasurface based on the genetic algorithm. The sound-absorption performance of the proposed metasurface is demonstrated by numerical simulation. The three subsurfaces of the proposed metasurface use the advantages of cavity resonance or local resonance in each frequency band. The excellent hydrostatic pressure resistance is realized due to the external steel wall. The thickness of the proposed metasurface is only 32 mm (not including the backboard), which has an advantage over the metasurfaces referenced in the previous paragraph.

II. DESIGN METHOD

An ultrathin underwater sound-absorption metasurface is designed based on a 32-mm anechoic layer, as shown in Fig. 1. The optimization parameters (d_1–d_{11}) are the geometric parameters of lead and the cavity; their sizes and shapes, as well as the distances from the steel wall, can be controlled. From top to bottom, the three subsurfaces are termed local-resonance subsurface 1 (LRS1), the cavity-resonance subsurface (CRS), and local-resonance subsurface 2 (LRS2), respectively. Due to the characteristic impedance of viscoelastic rubber being very close to that of water and its high viscosity, there can be a large consumption of sound energy. The local resonance and cavity resonance induced by lead and the cavity, respectively, in viscoelastic rubber have their own advantages of different frequency bands; thus, we consider coupling the two principles to achieve the broadband sound-absorption performance. The fixation of the external steel wall has a strong constraint on the internal viscoelastic rubber boundary. Under the action of underwater sound, the displacement modes of concave rubber, convex single rubber, convex double rubber, and so on occur on the fluid-structure coupling interface between viscoelastic rubber and water. Moreover, the constraint of the steel wall increases the stiffness of the rubber and makes it resistant to hydrostatic pressure. Detailed analyses are given in Sec. III C *and* Appendix B. The parameters (d_1–d_{11}) with excellent low-frequency and broadband sound-absorption effects are found by considering the strong global optimization ability of the genetic algorithm. The algorithm flow chart is shown in Fig. 2.

The sound-absorption coefficients at specific discrete frequency points are calculated at 0–10 000 Hz. $\sum \alpha_i$ is regarded as a target function. Here, α_i refers to the sound-absorption coefficient calculated at a single discrete frequency point. In the design space of ultrathin thickness (32 mm), it is difficult for local resonance to improve the sound-absorption coefficient within the kilohertz band, while cavity resonance can compensate for the flaw. To make the local-resonance frequency point move to low frequency to approach the cavity-resonance point for broadband high-efficiency absorption, the lead should be as large as possible. In addition, to achieve a high sound-absorption coefficient at high frequency, a smaller cavity allows more high-frequency sound waves to enter the viscoelastic rubber and be consumed. From this analysis, to narrow the search range, the solution model and constraint conditions are set as follows:

$$\text{such that}\begin{cases}\max \sum \alpha_i & \\ 8\ \text{mm} \le d_1 \le 14\ \text{mm}, & \\ 7\ \text{mm} \le d_3 \le 8.5\ \text{mm}, & d_3 \le d_2 \le 9.5\ \text{mm}, \\ 8\ \text{mm} \le d_4 \le 17\ \text{mm}, & \frac{d_4}{2} + 1\ \text{mm} \le d_6 \le 29\ \text{mm} - \frac{d_4}{2}, \\ 18\ \text{mm} \le d_5 \le 27\ \text{mm}, & \frac{d_5}{2} + 1\ \text{mm} \le d_7 \le 29\ \text{mm} - \frac{d_5}{2}, \\ 8\ \text{mm} \le d_8 \le 17\ \text{mm}, & \frac{d_8}{2} + 1\ \text{mm} \le d_{10} \le 29\ \text{mm} - \frac{d_8}{2}, \\ 18\ \text{mm} \le d_9 \le 27\ \text{mm}, & \frac{d_9}{2} + 1\ \text{mm} \le d_{11} \le 29\ \text{mm} - \frac{d_9}{2}. \end{cases}$$

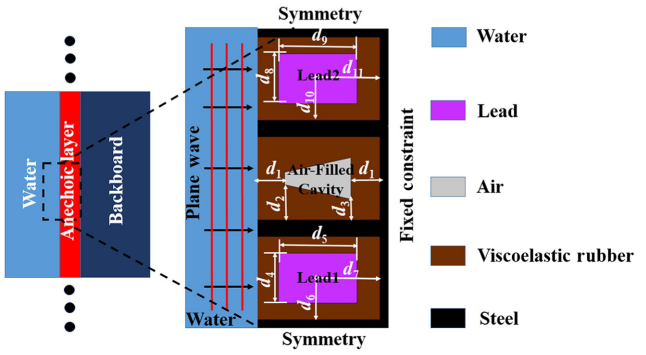

FIG. 1. Schematic diagram of ultrathin underwater sound-absorption metasurface.

No geometric intersection between lead, cavity, and the steel wall is realized under these constraints. The selection of discrete frequency points at relatively small intervals (every 200 Hz) over 0–4000 Hz is beneficial for improving the absorption coefficient of low- and middle-frequency bands. Similarly, the selection of discrete frequency points at relatively large intervals (every 400 Hz) over 4000–10 000 Hz also ensures the maintenance of an excellent sound-absorption coefficient for the high-frequency band. In the genetic algorithm, the population size is 60, the crossover probability (P_c) is 0.9, and the mutation probability (P_M) is 0.09. A large crossover probability is beneficial for the evolution of the population, while a small mutation probability ensures that the higher-order model of the population is not easily destroyed.

TABLE I. Material properties.

	Elastic modulus	Poisson ratio	Density (kg/m^3)	Loss factor	Sound speed (m/s)
Viscoelastic Rubber	21.4 MPa	0.47	1200	0.6	×
Lead	16.4 GPa	0.44	11 400	×	×
Steel	216 GPa	0.28	7850	×	×
Air	×	×	1.29	×	343
Water	×	×	1000	×	1500

The material parameters of the metasurface are shown in Table I. Here, the loss factor of viscoelastic rubber is set to 0.6, which is based on the fact that the loss of butyl rubber and neoprene rubber [11] can even exceed this value, and the frequency independence is also convenient for calculations.

III. RESULTS AND DISCUSSION

A. Convergence results of the genetic algorithm and calculation results for underwater sound absorption

The iterative process of the genetic algorithm is shown in Fig. 3(a). The population stops evolving at the 90th generation and tends to converge. The optimal individual of the 120th generation is chosen for the parameter values (d_1–d_{11}). The optimized parameter values and the sound-absorption coefficient curve are shown in Figs. 3(b) and 3(c). In the broadband range, the average sound-absorption

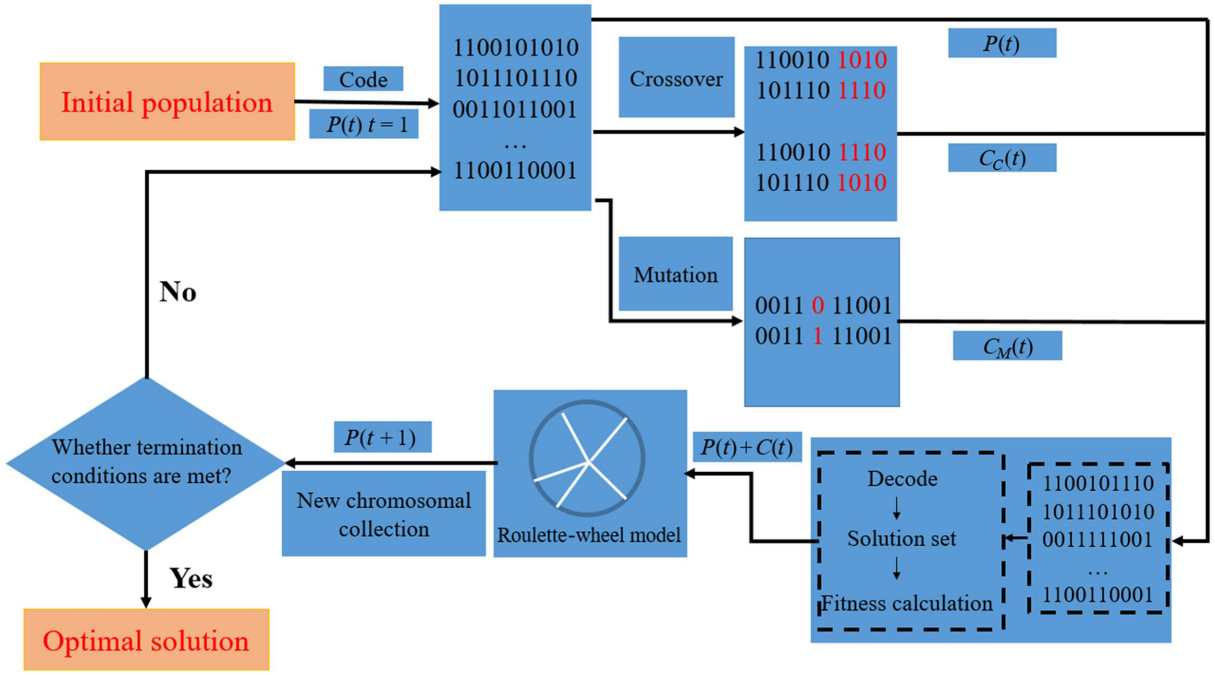

FIG. 2. Flow chart of the genetic algorithm (GA).

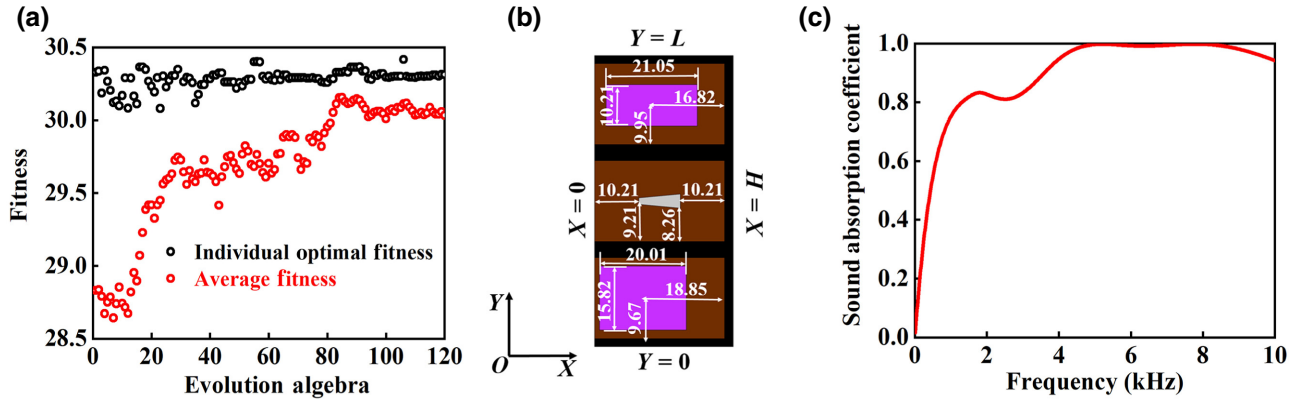

FIG. 3. (a) Iterative scatter diagram of the genetic algorithm. (b) Optimization results of parameters (d_1–d_{11}) with $L = 72$ mm and $H = 32$ mm. (c) Optimized sound-absorption coefficient curve.

coefficient can reach 89.3% at 0–10 000 Hz and 92.3% above 500 Hz, which includes an absorption coefficient of more than 95% at 4030–9820 Hz and more than 99% (nearly perfect absorption) at 4670–8630 Hz. In the low-frequency domain, the absorption coefficient can reach 60% at 580 Hz and 70% at 800 Hz. The metasurface shows excellent low-frequency and broadband underwater sound-absorption performance.

B. Influence of steel-wall thickness on underwater sound-absorption coefficient

In Sec. III A, the genetic algorithm is applied to optimize the parameters (d_1–d_{11}) on the basis of a steel-wall thickness of 2 mm. Different steel-wall thicknesses are selected to explore their influence on the underwater sound-absorption coefficient. The solution results are shown in Fig. 4. It is seen that, when the steel wall is thinner (<2 mm), the sound-absorption coefficient is higher at 0–1000 Hz, but the first sound-absorption resonance peak (around 2000 Hz) is low. Accordingly, when the steel wall is thicker (>2 mm), the sound-absorption coefficient decreases at 0–1000 and 3000–10 000 Hz, but the first sound-absorption resonance peak (around 2000 Hz) is higher. Therefore, from the perspective of the global sound-absorption coefficient, steel walls that are too thick or too thin (use 2 mm as a reference) have adverse effects. As the best of these outcomes, a steel-wall thickness of 2 mm is used in subsequent discussions.

C. Underwater low-frequency and broadband sound-absorption mechanism

The sound-absorption mechanism of the metasurface can be analyzed from the equivalent bulk modulus, B_{eff}; the equivalent mass density, ρ_{eff}; and the normalized impedance, Z_{eff}, to water. As shown in Fig. 3(b), the above equivalent parameters are calculated on the assumption that the medium between $X = 0$ and $X = H$ is homogeneous. These equivalent parameters can be calculated according to the transfer-matrix formula:

$$\begin{bmatrix} P_1 \\ V_1 \end{bmatrix} = \begin{bmatrix} \cos(k_{\text{eff}}H) & j\sin(k_{\text{eff}}H)\rho_{\text{eff}}c_{\text{eff}} \\ j\sin(k_{\text{eff}}H)/(\rho_{\text{eff}}c_{\text{eff}}) & \cos(k_{\text{eff}}H) \end{bmatrix} \begin{bmatrix} P_2 \\ V_2 \end{bmatrix}, \tag{1}$$

where k_{eff} is the equivalent wave number, c_{eff} is the equivalent sound velocity, and H is the distance from the incident boundary to the exit boundary. P_1 and P_2 are the normal stresses at the incident boundary and the exit boundary, respectively; V_1 and V_2 are the normal particle-vibration velocities at the incident boundary and the exit boundary, respectively. Here, P_1, P_2, V_1, and V_2 change along their respective boundaries. According to the equivalent-medium theory, they are extracted according to the average value of their respective boundaries. The exit boundary

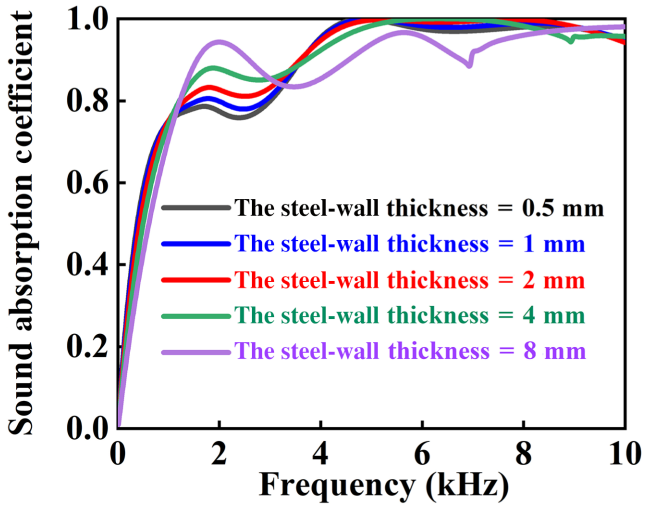

FIG. 4. Influence of steel-wall thickness on underwater sound-absorption coefficient.

is set as a fixed constraint, on account of connecting to the submarine surface, so $V_2 = 0$. Next, combined with the equation $B_{\text{eff}} = \rho_{\text{eff}} c_{\text{eff}}^2$, the equivalent bulk modulus, B_{eff}; the equivalent mass density, ρ_{eff}; and the normalized impedance, Z_{eff}, relative to water can be finally calculated as

$$
\begin{aligned}
Z_{\text{eff}} &= \frac{P_1}{V_1}, \\
\rho_{\text{eff}} &= \frac{\arccos(P_1/P_2)P_1}{(-j)\cot(\arccos(P_1/P_2))\omega H V_1}, \\
B_{\text{eff}} &= \frac{\omega H P_1}{(-j)\cot(\arccos(P_1/P_2))\arccos(P_1/P_2)V_1}.
\end{aligned} \tag{2}
$$

According to Eq. (2), related images are shown in Figs. 5(a)–5(c), respectively.

Next, the sound-absorption mechanism of the metasurface is analyzed for its excellent sound-absorption coefficient. As shown in Fig. 5(a), the change of the real part of the bulk-modulus curve is nonmonotone, which indicates the expansion and contraction of the metasurface volume. Furthermore, the change of the real part of the bulk modulus, B_{eff}, reflects the change in metasurface volume to explain the displacement modes of the metasurface. Corresponding to Fig. 5(a), the displacement modes of expansion and contraction of the metasurface at 0–10 000 Hz are plotted in Fig. 6. The imaginary part of the bulk modulus, B_{eff}, reflects the consumption ability for sound energy inside the metasurface, and the imaginary part of the mass density, ρ_{eff}, in Fig. 5(b) also plays a similar role. Since we focus on the interpretation of the sound-absorption coefficient by the displacement modes, we are concerned with the change of the real part of the bulk modulus, B_{eff}. We select point *A* (1650 Hz), point *B* (3680 Hz), point *C* (5480 Hz), and point *D* (7160 Hz) as critical points for the change rate of the real part of the bulk modulus, B_{eff}. The critical points divide the whole frequency band into 10–1650 Hz (*O*-*A* frequency band), 1650–3680 Hz (*A*-*B* frequency band), 3680–5480 Hz (*B*-*C* frequency band), 5480–7160 Hz (*C*-*D* frequency band), and 7160–10 000 Hz (*D*-*E* frequency band). The change rate of the real part of the bulk modulus, B_{eff}, near the critical-frequency-point *A* is different, but the trend is consistent, indicating the change of the displacement mode. The change rate of the real part of the bulk modulus, B_{eff}, near critical-frequency-point *B*, -point *C*, and point *D* is opposite, which also indicates the change of the displacement mode. The local maximum and minimum values of the metasurface volume are also implied at these critical frequency points. Then we analyze the displacement modes of the metasurface in each frequency band in detail. At 10–1650 Hz (*O*-*A* frequency band), the bulk modulus, B_{eff}, decreases at a small rate. The *x*-displacement fields of the metasurface at 920 and 1650 Hz are extracted, as shown in Figs. 6(a) and 6(b). The displacement modes are very similar, as represented by the indented rubber of LRS1, LRS2, and CRS. The concave rubber of LRS1, LRS2, and CRS is reduced as the frequency increases. At 1650–3680 Hz (*A*-*B* frequency band), the bulk modulus, B_{eff}, decreases faster than that at the *O*-*A* frequency band. This indicates that the displacement pattern of the metasurface is different from that at the *O*-*A* frequency band. The *x*-displacement fields of the metasurface at 1650, 1800, 2100, 2280, 2510, 2950, and 3680 Hz are extracted, as shown in Figs. 6(b)–6(h). It can be shown that the metasurface volume increases as the frequency increases. In this complex process, the main subdivision is divided into the following two processes. In the process from Figs. 6(b) to 6(d), the volume of the CRS increases rapidly and the concavity disappears. Meanwhile, the displacement of the lead moving outward increases, exhibiting a strong local resonance. In the process from Figs. 6(d) to 6(h), the rubber in the CRS protrudes outwards and the volume increases greatly, while the local-resonance effect of the lead in LRS1 and LRS2 is weakened and the rubber at the edge corner of LRS2 recesses inward. The metasurface still displays a rapid volume increase, because the volume of rubber protruding outwards is larger than that of the rubber recessing inwards. The absorption peak and the absorption valley exist for the *A*-*B* frequency band (at

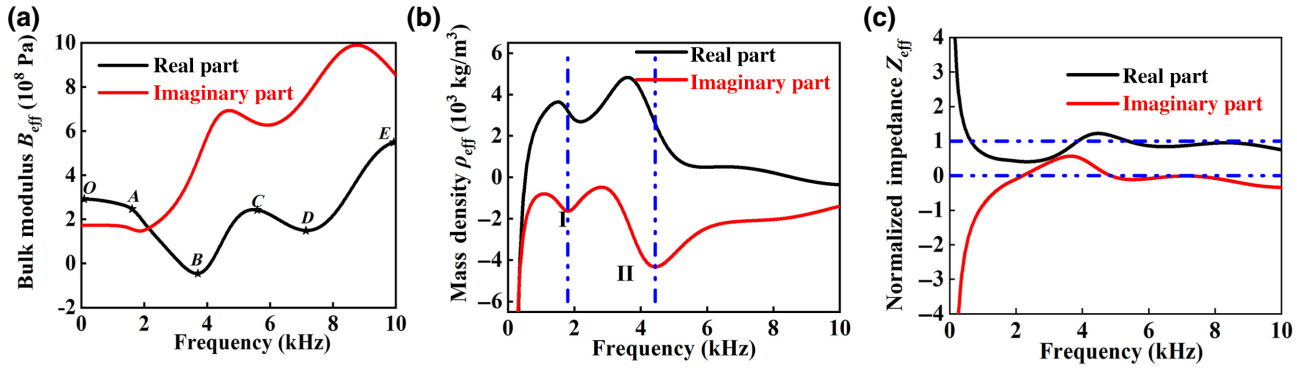

FIG. 5. (a) Equivalent bulk modulus, B_{eff}. (b) Equivalent mass density, ρ_{eff}. (c) Normalized impedance, Z_{eff}, relative to water.

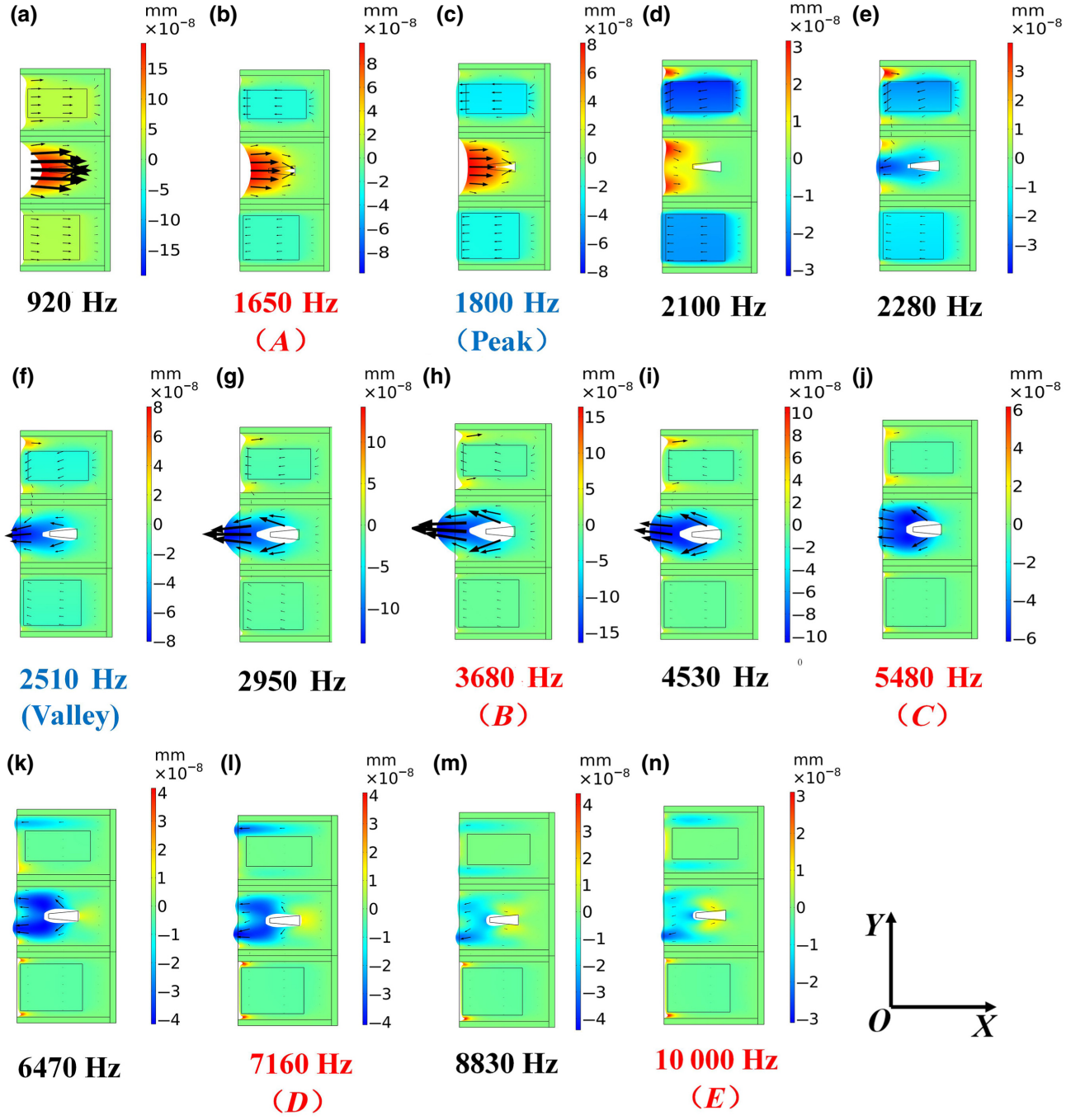

FIG. 6. Displacement field (magnified by 4×10^7) in the x direction of the metasurface at 0–10 000 Hz. (a) 920 Hz; (b) 1650 Hz; (c) 1800 Hz; (d) 2100 Hz; (e) 2280 Hz; (f) 2510 Hz; (g) 2950 Hz; (h) 3680 Hz; (i) 4530 Hz; (j) 5480 Hz; (k) 6470 Hz; (l) 7160 Hz; (m) 8830 Hz; (n) 10 000 Hz.

1800 and 2510 Hz respectively). At 1800 Hz, the outward motion of the lead reaches its maximum intensity and the local resonance is the strongest, so the absorption coefficient reaches its local maximum value. With an increase in frequency, the local resonance weakens and the absorption coefficient decreases gradually. However, it is observed that the rubber in the CRS gradually protrudes outward. As we can observed in Figs. 6(d)–6(h), the cavity resonance is gradually strengthened as the frequency increases, and particle displacement near the cavity is no longer horizontal, so there are components of y-direction (tangential) displacement. The y-direction (tangential) vibration of the rubber will lead to tangential loss, which is relatively larger than that of longitudinal loss. At 2510 Hz, the cavity

resonance compensates for the reduction of the absorption coefficient caused by local-resonance weakening. Therefore, the absorption coefficient rises rapidly due to the greater loss caused by the stronger cavity resonance when the frequency is higher than 2510 Hz. At 3680–5480 Hz (*B*-*C* frequency band), the bulk modulus, B_{eff}, increases at a large rate. The *x*-displacement fields of the metasurface at 3680, 4530, and 5480 Hz are also extracted, as shown in Figs. 6(h)–6(j). In this frequency band, the displacement modes of the volume decrease are shown. The central protruding large volume of rubber in the CRS gradually shrinks inward drastically and the rubber of the lower corner in the LRS1 recesses inward, but the concave rubber of the upper corner in LRS2 disappears. The sound-absorption coefficient increases gradually and remains very high. The main reason for this is that the loss caused by the cavity resonance and the concave rubber of the corner is enough to consume sound energy. At 5480–7160 Hz (*C*-*D* frequency band), the decreasing rate of the bulk modulus, B_{eff}, is slower than that of the *A*-*B* frequency band. This indicates that the metasurface volume changes less than the *A*-*B* frequency. The *x*-displacement fields of the metasurface at 5480, 6470, and 7160 Hz are extracted, as shown in Figs. 6(j)–6(l). In this frequency band, it shows that the displacement mode of the volume increases. The rubber in the CRS protrudes outward in the form of double small rubber petals. Meanwhile, the rubber in the upper corner of the LRS2 protrudes outward, but the rubber in the lower corner of the LRS1 recesses inward. Such a volume-change mode matches the sufficient shear-loss transformation in the high-frequency band without too much rubber protruding and recessing such that the sound-absorption coefficient always maintains nearly perfect absorption. At 7160–10 000 Hz (*D*-*E* frequency band), the bulk modulus, B_{eff}, increases again. The *x*-displacement fields of the metasurface at 7160, 8830, and 10 000 Hz are extracted, as shown in Figs. 6(l)–6(n). The rubber in the CRS contracts again, as does the rubber in the top corner in the LRS2. At 10 000 Hz, the rubber in the CRS has a tendency to protrude outward in a three-petal way. Over the whole volume-change process (0–10 000 Hz), the displacement modes are very rich, which can transform more sound waves into elastic waves. Especially, the large loss of the shear wave promotes sound absorption, resulting in the broadband high sound-absorption coefficient. For the equivalent density, ρ_{eff}, we pay more attention to its imaginary part, which reflects the dissipation of sound energy. The absorption peak usually appears at the local minimum point of the imaginary part of the equivalent mass density, ρ_{eff}. The local minimum points of the imaginary part of the equivalent mass density, ρ_{eff}, are obtained at point I (1800 Hz) and point II (4430 Hz), as shown in Fig. 5(b). In the absorption coefficient curve of the metasurface, the absorption peak is at point I (1800 Hz), but not at point II (4430 Hz). Furthermore, we observe that the real part of the equivalent mass density, ρ_{eff}, decreases at both 1800 and 4430 Hz. However, the difference between both frequencies is that the real part of the equivalent mass density, ρ_{eff}, at 4430 Hz decreases faster, resulting in a relatively large imaginary part. Therefore, the loss at 4430+ Hz (slightly greater than 4430 Hz) is likely to be higher than the loss at 4430 Hz, so point II (4430 Hz) is not the absorption peak. For the normalized impedance, Z_{eff}, relative to water, as shown in Fig. 5(c), the real part is approaching 1 and the imaginary part is close to 0 at 4000 Hz, which effectively confirms the perfect absorption characteristics of the broadband.

The sound-absorption coefficients of the three subsurfaces are compared with that of the metasurface, as shown in Fig. 7. Each subsurface has its respective advantage of a specific frequency band. The sound-absorption coefficient of the CRS has more advantages over LRS1 and LRS2 around 10–1000 and 5200–9300 Hz. Accordingly, LRS1 and LRS2 have higher absorption coefficients at around 1000–3920 Hz due to their respective local-resonance peaks. Under the ultrathin thickness of 32 mm, the size of lead is too limited to improve the absorption coefficient at low frequency. However, the cavity resonance can improve the sound-absorption coefficient at low frequency, which covers the deficiency of the local resonance. Moreover, the cavity resonance can improve the absorption coefficient at high frequency. However, the cavity resonance also has the disadvantage of the sound-absorption valley. The position of the local-resonance frequency point is adjusted near the cavity-resonance valley, which is beneficial for compensating for the weakness of the cavity resonance. The three subsurfaces optimized by the genetic algorithm are the embodiment of the complementary advantages of local resonance and cavity resonance. At 1800 Hz, the metasurface reaches the resonance peak ($\alpha = 0.83$). LRS1 and LRS2 also realize an almost-perfect absorption resonance peak (the actual resonant frequency points of both are 1690 and 1850 Hz), while the CRS

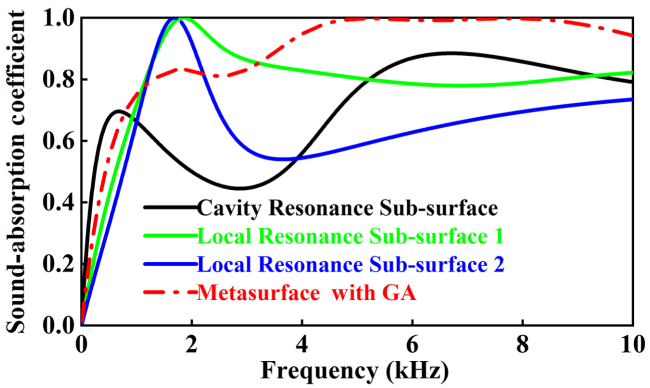

FIG. 7. Sound-absorption-coefficient curves of the metasurface and subsurfaces.

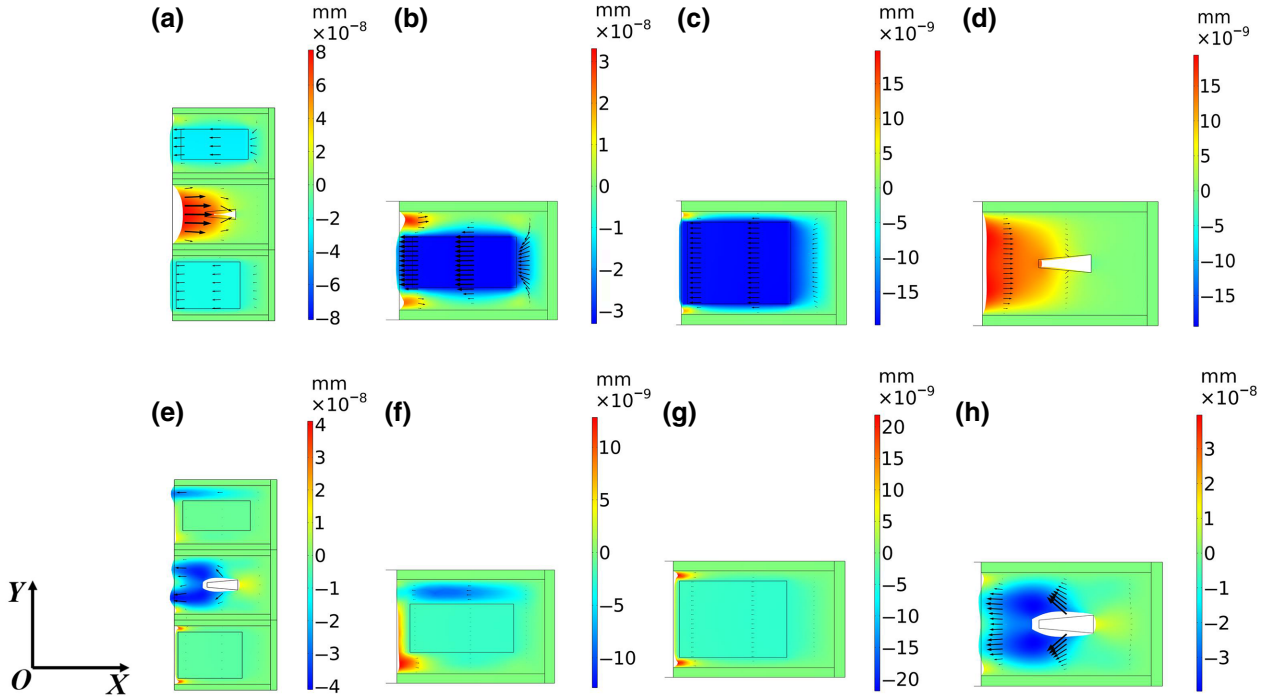

FIG. 8. The x-direction displacement field (magnified by 4×10^7) of (a) metasurface, (b) LRS2, (c) LRS1, and (d) CRS at 1800 Hz. The x-direction displacement field of (e) metasurface, (f) LRS2, (g) LRS1, and (h) CRS at 6720 Hz.

has a low absorption coefficient. The x-direction displacement fields of the metasurface and three subsurfaces are extracted at 1800 Hz, as shown in Figs. 8(a)–8(d). The metasurface and three subsurfaces have similar displacement fields, but the intensities are different. For the CRS in the metasurface, the rubber still vibrates in the displacement mode of indention, and the indention degree is much greater than that of the single CRS, as shown in Figs. 8(a) and 8(d). The large indention degree indicates that the equivalent stiffness of the metasurface is low, which improves the absorption coefficient of the metasurface at low frequency. This reveals that the coupling effect between the three subsurfaces reduces the equivalent stiffness of the CRS, and thus, improves the sound absorption of the metasurface at 1800 Hz. At 6720 Hz, the sound-absorption coefficient of the CRS reaches the maximum value ($\alpha = 0.88$). The displacement fields of the metasurface and subsurfaces are extracted, as shown in Figs. 8(e)–8(h). Similarly, the metasurface and three subsurfaces have similar displacement fields, but the intensities are different. The CRS in the metasurface protrudes with a larger volume than that of the single CRS, as shown in Figs. 8(e) and 8(h). Moreover, the rubber in the upper corner of the LRS2 in the metasurface protrudes outwards, while the rubber at the corresponding position in the single LRS2 [Fig. 8(f)] only has a tendency to protrude. The rubber protruding excessively from the metasurface increases the sound-energy loss to make the sound-absorption coefficient of the metasurface extremely high. Overall, the coupling between the three subsurfaces plays an important role in improving the sound-absorption coefficient of the metasurface.

To illustrate the effectiveness of this design, the metasurface is compared with other representative underwater sound-absorption metasurfaces reported in the literature [12,31,32]. As shown in Fig. 9, the design in this article has great advantages in terms of thickness, thickness-to-wavelength ratio, and sound-absorption bandwidth, which proves the excellence of the proposed metasurface in terms of sound-absorption performance.

D. Coupling analysis of subsurfaces based on the equivalent-circuit model

For the underwater sound-absorbing metasurface and three subsurfaces (LRS1, CRS, and LRS2), the normalized surface impedances can be denoted as Z_1, Z_2, Z_3, and Z_s. The detailed finite-element calculation of Z_i ($i = 1$, 2, 3, s) is given in Appendix A. As shown in Fig. 10, the coupling mechanism is furthermore explained by the equivalent-circuit model. Z_s is calculated via equivalent-circuit parallel addition as

$$Z_s = \frac{L}{\sum_{k=1}^{3} L_i/Z_i}, \tag{3}$$

where L refers to the total width of the two-dimensional metasurface and L_i to the width of each subsurface. We know that $\mathrm{Re}(Z_s) \to 1$ and $\mathrm{Im}(Z_s) \to 0$ are required to

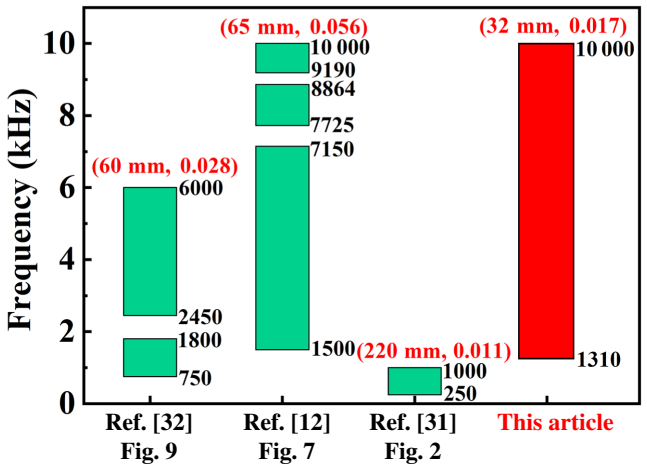

FIG. 9. Comparison of the thickness, thickness-to-wavelength ratio (0.7 of sound-absorption coefficient), and sound-absorption bandwidth (over 0.8 of sound-absorption coefficient) of the underwater sound-absorption metasurface with those in other representative references. First term in brackets is the metasurface thickness, and second term is the thickness wavelength ratio.

achieve a high sound-absorption coefficient, α. α is calculated based on

$$\alpha = \frac{4\,\mathrm{Re}(Z_s)}{[1+\mathrm{Re}(Z_s)]^2 + \mathrm{Im}(Z_s)^2} \tag{4}$$

However, the dispersion relationship of the actual three impedances (Z_1, Z_2, and Z_3) is difficult to deduce to fit $\mathrm{Re}(Z_s)\to 1$ and $\mathrm{Im}(Z_s)\to 0$. The method of searching for suitable d_1–d_{11} to match high sound-absorption coefficients also searches for suitable dispersion relationships for Z_1, Z_2, and Z_3 to realize the flat impedance, Z_s [$\mathrm{Re}(Z_s)\to 1$, $\mathrm{Im}(Z_s)\to 0$]. Therefore, the optimal acquisition of Z_1, Z_2, and Z_3 can be realized by controlling the iteration of the sound-absorption coefficient with the genetic algorithm.

In the analysis of Sec. III C, LRS1 and LRS2 achieve nearly perfect absorption at 1690 and 1850 Hz, respectively. As shown in Fig. 11, the impedances of LRS1 and LRS2 at 1690 and 1850 Hz are $Z_{\mathrm{LRS1}}|_{\omega=1690\ \mathrm{Hz}} = 1.038\,64 + 0.004\,94j$ and $Z_{\mathrm{LRS2}}|_{\omega=1850\ \mathrm{Hz}} = 0.973\,44 + 0.023\,05j$, respectively, which conforms to $\mathrm{Re}(Z_n)\to 1$ and $\mathrm{Im}(Z_n)\to 0$. Therefore, the nearly perfect absorption of LRS1 and LRS2 is verified. In addition, although the resonant frequency points of LRS1 and LRS2 are relatively close, the impedances of the two are very different for the whole frequency band. According to Eq. (3), the direct parallel summation of $1/Z_n$ is still possible to realize $\mathrm{Re}(Z_s)\to 1$ and $\mathrm{Im}(Z_s)\to 0$. The flat impedance generated by direct parallel summation of $1/Z_n$ is confirmed, and the result is shown in Fig. 5(c). This indicates that the genetic algorithm achieves appropriate acquisition of Z_1, Z_2, and Z_3 to generate flat impedance. Moreover, the flat impedance at 4670–8630 Hz almost conforms to $\mathrm{Re}(Z_s)\to 1$ and $\mathrm{Im}(Z_s)\to 0$, and the corresponding nearly perfect absorption is also the contribution from the genetic algorithm. Overall, the coupling between subsurfaces is essentially a flat impedance acquisition via direct parallel summation with appropriate $1/Z_n$ selection.

E. Influence of out-of-plane thickness on the sound-absorption coefficient

As shown in Fig. 12, the three-dimensional model is placed on the surface of the steel backing in the impedance tube. The thicker steel backing (>10 mm) not only makes the transmission almost zero, but also reflects the sound

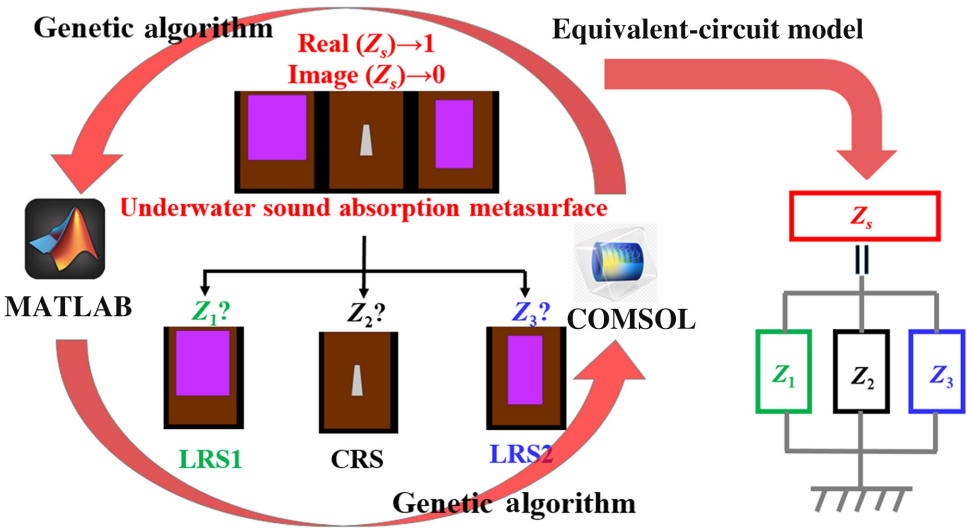

FIG. 10. Impedance designs of underwater sound-absorption metasurface based on the genetic algorithm.

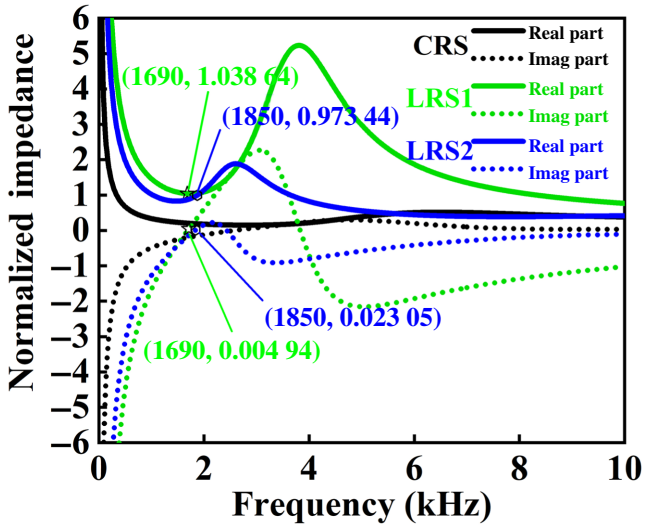

FIG. 11. Normalized surface-impedance acquisition of CRS, LRS, and LRS2.

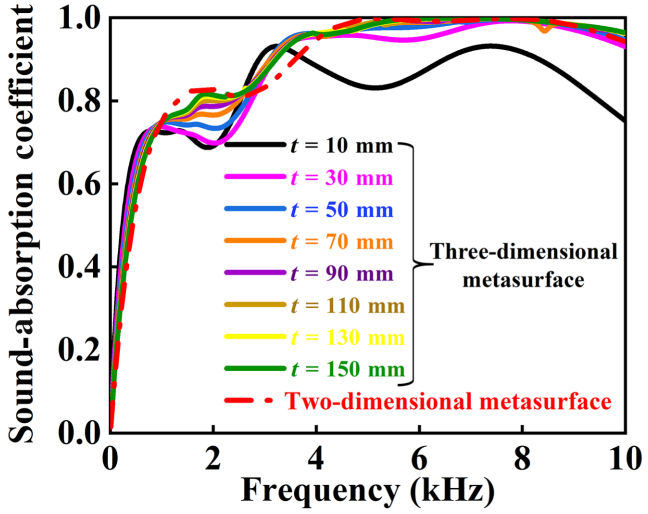

FIG. 13. Comparison of sound-absorption coefficient with a two-dimensional model under different out-of-plane thicknesses.

pressure almost completely, so that the metasurface can absorb the sound energy twice. The reflected sound pressure of the metasurface should be extracted far away from the metasurface to ensure the uniformity of the sound-pressure distribution. The influence of the out-of-plane thickness on the sound-absorption coefficient is investigated. As shown in Fig. 13, the metasurface is closer to the plane-stress state when $t = 10$ mm, so that the sound-absorption coefficient is quite different from the two-dimensional model (plane-strain state). In the three-dimensional metasurface shown in Fig. 12, there must be gaps between the impedance tube and the front and rear surfaces of the metasurface along the out-of-plane thickness direction; thus, two free surfaces must be generated. The stiffness of the metasurface is lowest near the two free surfaces. With an increase in the out-of-plane thickness, the decrease of the low-frequency (within kilohertz) sound-absorption coefficient is caused by the increase of the equivalent stiffness of the metasurface, which derives from the decrease of the proportion of the low-stiffness region. Furthermore, the absorption coefficient converges to the two-dimensional model gradually with an increase of the out-of-plane thickness, which also confirms that the essence of the two-dimensional metasurface is a three-dimensional model with infinite out-of-plane thickness. On account of the actual anechoic overlay having a large size in both dimensions of the laying area, the two-dimensional metasurface can be well applied to practical scenarios by virtue of its characteristic of infinite length.

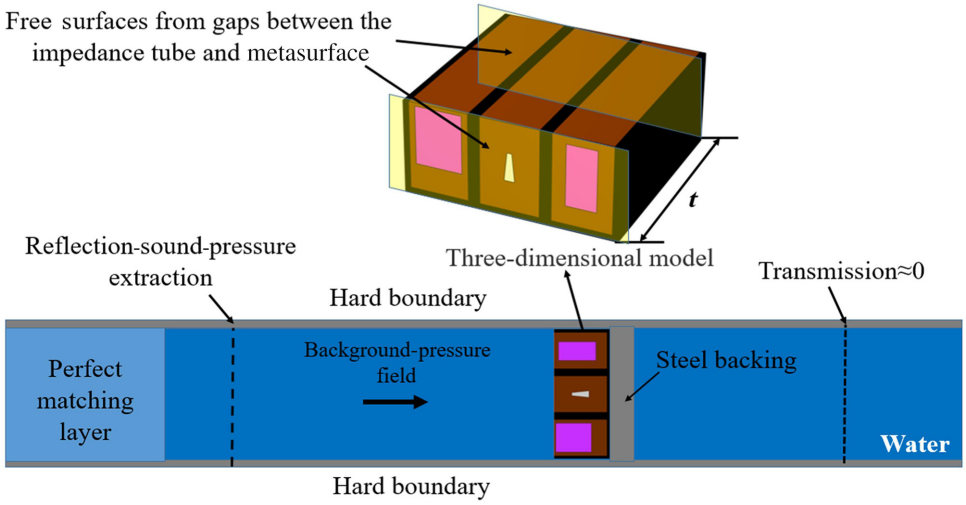

FIG. 12. Three-dimensional model of underwater sound-absorption metasurface tested by the impedance tube.

IV. CONCLUSION

Here, we stitch three subsurfaces in a parallel way to form an underwater sound metasurface to achieve excellent low-frequency and broadband sound absorption. The coupling of local resonance and cavity resonance is the key to the high-efficiency sound absorption. The average sound-absorption coefficient can reach 89.3% at 0–10 000 Hz (92.3% above 500 Hz) for the broadband, 60% at 580 Hz, and 70% at 800 Hz for low frequency. The bulk modulus, B_{eff}; mass density, ρ_{eff}; and normalized impedance, Z_{eff}, extracted by the transfer-matrix method can explain the sound-absorption mechanism effectively. The related displacement fields of the metasurface and three subsurfaces also demonstrate the coupling of each subsurface. Furthermore, the equivalent-circuit model is used to further confirm the coupling relationship between the metasurface and three subsurfaces. Moreover, the excellent performance of high-efficiency sound absorption is maintained under 4.5-MPa hydrostatic pressure. The proposed underwater sound-absorption metasurface may open up a route for application in the field of underwater noise reduction.

All data included in this study are available upon request from the corresponding author.

ACKNOWLEDGMENT

The authors are grateful for support from the National Natural Science Foundation of China (Grant No. 51575431).

APPENDIX A: SURFACE-IMPEDANCE CALCULATION OF THE METASURFACE BASED ON THE FINITE-ELEMENT METHOD

The finite-element method for surface-impedance calculation of the metasurface is as follows.

The equation for the sound wave in water can be expressed as

$$\frac{1}{c}\frac{\partial^2 p}{\partial t^2} = \nabla^2 p, \tag{A1}$$

where t denotes time, p is sound pressure, and c represents sound speed. For the fluid-structure coupling interface, the particle velocity in water is equal to the particle velocity in the metasurface, as given by

$$\rho_0 \frac{\partial u}{\partial t} = -\nabla p. \tag{A2}$$

The water area and the metasurface are discretized by the finite-element method, and the equations satisfied by each discrete unit are expressed as

$$\begin{aligned} M_{\text{water}}\frac{\partial^2 p}{\partial t^2} + K_{\text{water}} p + \rho_0 R\frac{\partial^2 u}{\partial t^2} &= F_p, \\ M_{\text{metasurface}}\frac{\partial^2 u}{\partial t^2} + K_{\text{metasurface}} u - R^T\frac{\partial^2 p}{\partial t^2} &= F_m, \end{aligned} \tag{A3}$$

where M_{water}, K_{water}, and F_p refer to the mass matrix, stiffness matrix, and external force of each node of the element body in water area, respectively. $M_{\text{metasurface}}$, $K_{\text{metasurface}}$, and F_m refer to the mass matrix, stiffness matrix, and external force of each node of the element body in the metasurface, respectively. R represents the interaction between water area and the metasurface at the fluid-structure interface. By assembling the finite-element equations of each element body, the total solution equation is described as

$$\begin{bmatrix} K_{\text{metasurface}} - \omega^2 M_{\text{metasurface}} & R^T \\ -\rho_0\omega_2 R & K_{\text{water}} - C_g - \omega^2 M_{\text{water}} \end{bmatrix} \times \begin{bmatrix} u \\ p \end{bmatrix} = \begin{bmatrix} F_m \\ F_p \end{bmatrix}, \tag{A4}$$

where C_g contains the sound normal pressure gradient in the truncation surfaces of the semi-infinite water domain [7]. Combined with Fig. 3(b), the boundary conditions are written as follows:

$$\begin{aligned} &\text{fixed constraint, } u_{//}|_{X=H} = 0,\ u_{\perp}|_{X=H} = 0, \\ &\text{symmetry, } u_{\perp}|_{Y=0} = 0,\ u_{\perp}|_{Y=L} = 0. \end{aligned} \tag{A5}$$

Combined with Eqs. (A1)–(A5), the sound pressure and displacement at the fluid-structure coupling interface can be solved. Therefore, surface impedance, Z_s, of the metasurface can be calculated as

$$Z_s = \frac{p|_{X=0}}{u_{\perp}|_{X=0} Z_{\text{water}}},$$

where Z_{water} refers to the characteristic impedance of water. Accordingly, Z_1, Z_2, and Z_3 can be calculated by using a similar method.

APPENDIX B: ANALYSIS OF THE SOUND-ABSORPTION COEFFICIENT OF THE METASURFACE UNDER HYDROSTATIC PRESSURE

The hydrostatic pressure resistance of the metasurface is analyzed. The metasurface is deformed under 3- and 4.5-MPa hydrostatic pressures, as shown in Figs. 14(a) and 14(b). At 3 MPa, the steel wall hardly deforms. Moreover, the deformation of the rubber is also very small due to the support of the external steel wall. The deformation of the rubbers in the three subsurfaces are calculated. The deformation is mainly concentrated on the left boundary (plane-wave incidence boundary). The compressive

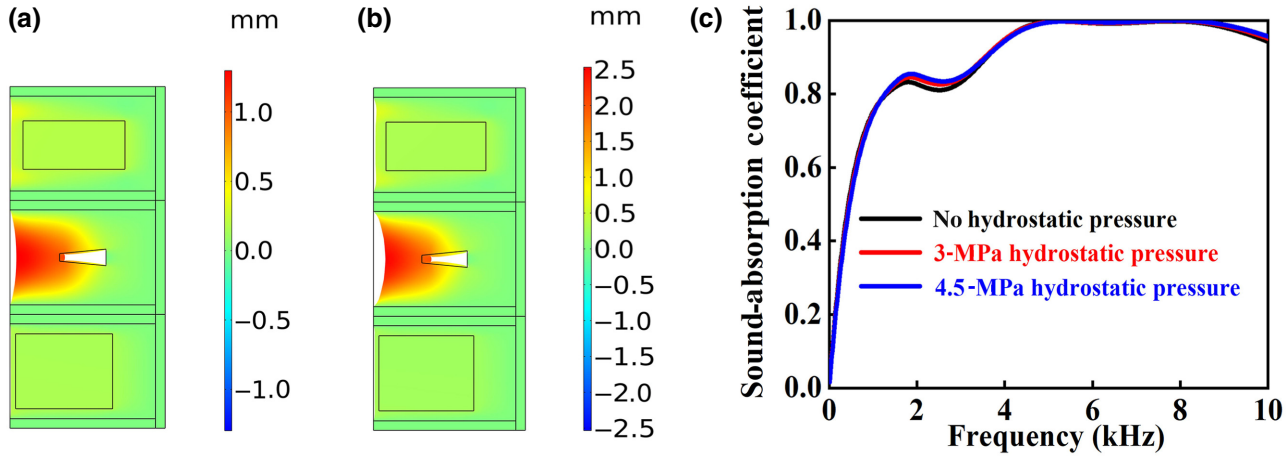

FIG. 14. (a) The x-direction displacement field of the metasurface at 3-MPa hydrostatic pressure. (b) The x-direction displacement field of the metasurface at 4.5-MPa hydrostatic pressure. (c) Sound-absorption coefficient of the metasurface without hydrostatic pressure and with hydrostatic pressure (3 and 4.5 MPa).

displacements of the left boundary of the three subsurfaces are calculated as 0.27, 0.91, and 0.17 mm (the compressive strains are 0.9%, 3.03%, and 0.6%, respectively). Therefore, the hydrostatic pressure mainly has a slight densification effect on the rubber. Under the condition of compression deformation, the sound-absorption coefficients are calculated, as shown in Fig. 14(c). The densification of rubber and the change of the rubber's geometric shape make the sound-absorption coefficient near the local-resonance peak slightly increase, and the other sound-absorption frequency bands have little influence. Compared with no hydrostatic pressure, the resonance frequency moves slightly to higher frequency (from 1800 to 1840 Hz), but the absorption coefficient increases only a little (from 0.833 to 0.846). Similarly, the deformation under a hydrostatic pressure of 4.5 MPa is slightly larger than that under a hydrostatic pressure of 3 MPa. Compared with the absorption coefficient at 3 MPa, there is still a slight difference near the local-resonance peak (the absorption coefficient is 0.855 at 1870 Hz). In the low-frequency band (before the local-resonance peak frequency), the absorption coefficient decreases slightly. In the high-frequency band, the absorption coefficient also rises slightly. In general, supported by steel walls, the metasurface has a high hydrostatic pressure resistance, and hydrostatic pressures of 3 and 4.5 MPa have little influence on the sound-absorption performance.

[1] M. Chen, D. Meng, H. Zhang, H. Jiang, and Y. R. Wang, Resonance-coupling effect on broad band gap formation in locally resonant sonic metamaterials, Wave Motion **63**, 111 (2016).

[2] J. Wen, H. Zhao, L. Lv, B. Yuan, G. Wang, and X. Wen, Effects of locally resonant modes on underwater sound absorption in viscoelastic materials, J. Acoust. Soc. Am. **130**, 1201 (2011).

[3] Y. Zhang, J. Pan, K. Chen, and J. Zhong, Subwavelength and quasi-perfect underwater sound absorber for multiple and broad frequency bands, J. Acoust. Soc. Am. **144**, 648 (2018).

[4] J. Duan, S. Li, X. Wu, C. Wang, and Y. Ma, A new eccentric resonance matching layer with anti-reflection characteristics for underwater acoustic scattering suppression, Phys. Scr. **96**, 035001 (2020).

[5] T. Wang, J. Liu, and M. Chen, Underwater sound absorption of a meta-absorption layer with double negativity, Appl. Acoust. **181**, 108182 (2021).

[6] G. S. Sharma, A. Skvortsov, I. MacGillivray, and N. Kessissoglou, Sound absorption by rubber coatings with periodic voids and hard inclusions, Appl. Acoust. **143**, 200 (2019).

[7] G. Jin, K. Shi, T. Ye, J. Zhou, and Y. Yin, Sound absorption behaviors of metamaterials with periodic multi-resonator and voids in water, Appl. Acoust. **166**, 107351 (2020).

[8] H. Meng, J. Wen, H. Zhao, L. Lv, and X. Wen, Analysis of absorption performances of anechoic layers with steel plate backing, J. Acoust. Soc. Am. **132**, 69 (2012).

[9] J. Zhong, H. Zhao, H. Yang, J. Yin, and J. Wen, On the accuracy and optimization application of an axisymmetric simplified model for underwater sound absorption of anechoic coatings, Appl. Acoust. **145**, 104 (2019).

[10] G. S. Sharma, A. Skvortsov, I. MacGillivray, and N. Kessissoglou, Acoustic performance of gratings of cylindrical voids in a soft elastic medium with a steel backing, J. Acoust. Soc. Am. **141**, 4694 (2017).

[11] Y. Fu, I. I. Kabir, G. H. Yeoh, and Z. Peng, A review on polymer-based materials for underwater sound absorption, Polym. Test. **96**, 107115 (2021).

[12] Z. Wang, Y. Huang, X. Zhang, L. Li, M. Chen, and D. Fang, Broadband underwater sound absorbing structure with gradient cavity shaped polyurethane composite array supported by carbon fiber honeycomb, J. Sound Vib. **479**, 115375 (2020).

[13] K.-I. Jung, S. W. Yoon, S.-J. Sung, and J.-K. Park, Carbon black effect on the acoustic properties of nitrile butadiene rubber, J. Appl. Polym. Sci. **94**, 678 (2004).
[14] T. Yu, F. Jiang, J. Wang, Z. Wang, Y. Chang, and C. Guo, Acoustic insulation and absorption mechanism of metallic hollow spheres composites with different polymer matrix, Compos. Struct. **248**, 112566 (2020).
[15] H. Zhong, Y. Gu, B. Bao, Q. Wang, and J. Wu, 2D underwater acoustic metamaterials incorporating a combination of particle-filled polyurethane and spiral-based local resonance mechanisms, Compos. Struct. **220**, 1 (2019).
[16] Y. Gu, H. Zhong, B. Bao, Q. Wang, and J. Wu, Experimental investigation of underwater locally multi-resonant metamaterials under high hydrostatic pressure for low frequency sound absorption, Appl. Acoust. **172**, 107605 (2021).
[17] Y. Zhang, H. Huang, J. Zheng, and J. Pan, Underwater sound scattering and absorption by a coated infinite plate with attached periodically located inhomogeneities, J. Acoust. Soc. Am. **138**, 2707 (2015).
[18] G. S. Sharma, A. Skvortsov, I. MacGillivray, and N. Kessissoglou, Acoustic performance of periodic steel cylinders embedded in a viscoelastic medium, J. Sound Vib. **443**, 652 (2019).
[19] H. Meng, J. Wen, H. Zhao, and X. Wen, Optimization of locally resonant acoustic metamaterials on underwater sound absorption characteristics, J. Sound Vib. **331**, 4406 (2012).
[20] Z. Zhang, J. Wang, and Q. Huang, A novel semi-analytical methodology for predicting sound absorption of anechoic coatings with arbitrary rotary cavities dependent on temperature and frequency, Results Phys. **26**, 104408 (2021).
[21] C. Ye, X. Liu, F. Xin, and T. J. Lu, Influence of hole shape on sound absorption of underwater anechoic layers, J. Sound Vib. **426**, 54 (2018).
[22] D. C. Calvo, A. L. Thangawng, C. N. Layman, Jr., R. Casalini, and S. F. Othman, Underwater sound transmission through arrays of disk cavities in a soft elastic medium, J. Acoust. Soc. Am. **138**, 2537 (2015).
[23] S. M. Ivansson, Numerical design of Alberich anechoic coatings with superellipsoidal cavities of mixed sizes, J. Acoust. Soc. Am. **124**, 1974 (2008).
[24] D. Zhao, H. Zhao, H. Yang, and J. Wen, Optimization and mechanism of acoustic absorption of Alberich coatings on a steel plate in water, Appl. Acoust. **140**, 183 (2018).
[25] V. Leroy, A. Strybulevych, M. Lanoy, F. Lemoult, A. Tourin, and J. H. Page, Superabsorption of acoustic waves with bubble metascreens, Phys. Rev. B **91**, 020301(R) (2015).
[26] S. M. Ivansson, Sound absorption by viscoelastic coatings with periodically distributed cavities, J. Acoust. Soc. Am. **119**, 3558 (2006).
[27] X. An, C. Lai, W. He, and H. Fan, Three-dimensional chiral meta-plate lattice structures for broad band vibration suppression and sound absorption, Composites, Part B **224**, 109232 (2021).
[28] Y. Gu, H. Long, Y. Cheng, M. Deng, and X. Liu, Ultrathin Composite Metasurface for Absorbing Subkilohertz Low-Frequency Underwater Sound, Phys. Rev. Appl. **16**, 014021 (2021).
[29] M. Duan, C. Yu, F. Xin, and T. J. Lu, Tunable underwater acoustic metamaterials via quasi-Helmholtz resonance: From low-frequency to ultra-broadband, Appl. Phys. Lett. **118**, 071904 (2021).
[30] H. Wu, H. Zhang, and C. Hao, Reconfigurable spiral underwater sound-absorbing metasurfaces, Extreme Mech. Lett. **47**, 101361 (2021).
[31] N. Gao and Y. Zhang, A low frequency underwater metastructure composed by helix metal and viscoelastic damping rubber, J. Vib. Control **25**, 538 (2018).
[32] Y. Zhang and L. Cheng, Ultra-thin and broadband low-frequency underwater acoustic meta-absorber, Int. J. Mech. Sci. **210**, 106732 (2021).
[33] L. B. Wang, C. Z. Ma, and J. H. Wu, A thin metastructure with multi-order resonance for underwater broadband sound absorption in low frequency, Appl. Acoust. **179**, 108025 (2021).